A wider look at the gravitational-wave transients from GWTC-1 using an unmodeled reconstruction method

F. Salemi,[1] E. Milotti,[2] G. A. Prodi,[3,4] G. Vedovato,[5]
C. Lazzaro,[6] S. Tiwari,[7] S. Vinciguerra,[1]
M. Drago,[8,9] and S. Klimenko[10]

[1] *Albert-Einstein-Institut, Max-Planck-Institut für Gravitationsphysik, D-30167 Hannover, Germany*
[2] *Dipartimento di Fisica, Università di Trieste and INFN Sezione di Trieste, Via Valerio, 2, I-34127 Trieste, Italy*
[3] *Università di Trento, Dipartimento di Fisica, I-38123 Povo, Trento, Italy*
[4] *INFN, Trento Institute for Fundamental Physics and Applications, I-38123 Povo, Trento, Italy*
[5] *INFN, Sezione di Padova, I-35131 Padova, Italy*
[6] *Università di Padova, Dipartimento di Fisica e Astronomia, I-35131 Padova, Italy*
[7] *Physik-Institut, University of Zurich, Winterthurerstrasse 190, 8057 Zurich, Switzerland*
[8] *Gran Sasso Science Institute, Via F. Crispi 7, I-67100, L'Aquila, Italy*
[9] *INFN, Laboratori Nazionali del Gran Sasso, I-67100 Assergi, Italy*
[10] *University of Florida, Gainesville, FL 32611, USA*

(Dated: May 23, 2019)

In this paper, we investigate the morphology of the events from the GWTC-1 catalog of compact binary coalescences as reconstructed by a generic method based on coherent excess power: we use an open-source version of the coherent WaveBurst (cWB) analysis pipeline, which does not rely on the detailed knowledge of the waveform models. cWB extracts the coherent response of the detectors' network to a generic gravitational wave, using loose bounds on the duration and bandwidth of the signal. This pipeline version reproduces the same results that were reported for cWB in recent publications by the LIGO and Virgo collaborations. The sky localization and waveform reconstruction performed by cWB are in a good agreement with the most accurate parameter estimates currently available, i.e. those produced by methods which exploit the detailed theoretical knowledge of the expected waveform for compact binary coalescences. However, in some cases cWB also detects features in excess in well-localized regions of the time-frequency plane. We have then devised and implemented a procedure to assess the probability that such deviations are significant. Out of the eleven events reported in the GWTC-1, there are two cases – the events GW151012 and GW151226 – where cWB detects an excess of coherent energy after the merger ($\Delta t \simeq 0.2$ s and $\simeq 0.1$ s, respectively) with p-values that call for further investigations (0.004 and 0.03, respectively), though they are not sufficient to exclude noise fluctuations. We discuss the morphological properties and plausible interpretations of these features. We believe that the methodology described in the paper shall be useful in future searches and we look forward to its application to the the events of the ongoing observing run of the LIGO-Virgo Collaboration.

PACS numbers: 04.80.Nn, 04.25.dg, 95.85.Sz,

I. INTRODUCTION

Gravitational-wave (GW) astrophysics is successfully gearing up and producing a wealth of unprecedented results, among which the gravitational-wave transient catalog (GWTC-1) of compact binary coalescences (CBC) [1]) from the recent observing runs of the Advanced LIGO [2] and Advanced Virgo [3] detectors and the tests of gravity in previously unaccessible regimes [4]. Template-based methods, which use Bayesian inference, are indeed producing astonishing results([5]). In particular, these analyses are unveiling the intrinsic properties of the binary black hole mergers, such as masses and spins, thanks to their well-understood theoretical models and their clearly recognizable waveforms (see, e.g., [6–8]).

In our work, we investigate the morphology of the events from the GWTC-1 catalog of compact binary coalescences as reconstructed by an alternative approach that does not depend on specific models, but rather extracts the coherent response of the detector network to generic gravitational waves and uses only very loose additional bounds on the duration and bandwidth of the signal. This methodology is robust with respect to a variety of well-known CBC signal features including the higher order modes [9], high mass ratios, misaligned spins, eccentric orbits and complements the existing template-based algorithms by searching for new and possibly unexpected CBC populations/waveform features. The present analysis extends the well-established analyses reported in [1, 4] by looking for features that add to the conventional CBC signal models, especially at times after coalescence.

In section II A, we briefly introduce *coherent WaveBurst* (cWB), an unmodeled algorithm for searching and reconstructing GW transients and its open source version [1] which we adopted for the production of all results reported in this paper. In section II B, we introduce the

[1] cWB home page, `https://gwburst.gitlab.io/`;

Monte Carlo simulation that we used to estimate all relevant deviations for our estimations. Section III illustrates the cWB reconstruction capabilities on the set of GW events from the GWTC-1 [1]. We summarize the main features of the events in GWTC-1 and compare the reconstructed sky localizations of the sources and waveforms to those provided by methods based on signal templates [2]. Follow-up studies on the two main outliers – the events GW151012 and GW151226 – where cWB detects an excess of coherent energy after coalescence – are reported in section III C. Finally, in section IV we discuss plausible interpretations for the observed deviations in the reconstructed waveforms for GW151012 and for GW151226, and we conclude the paper with a very brief discussion of the perspectives for further studies that are opened up by the increased sensitivity of the advanced detectors in the ongoing LIGO-Virgo survey [11].

II. METHODS

A. coherent WaveBurst

Coherent Waveburst (cWB) [12] is an analysis algorithm used in searches for generic transient signals with networks of GW detectors. Designed to operate without a specific waveform model, cWB first identifies coincident excess power in the multi-resolution time-frequency representations of the detectors strain data and then it reconstructs events which are coherent in multiple detectors as well as the source sky location and signal waveform: by using the constrained maximum likelihood method [13] it combines all data streams into one coherent statistic η_c based on the coherent energy E_c, i.e., $\eta_c \propto \sqrt{E_C}$, which is proportional to the coherent signal-to-noise ratio (SNR) in the detector network and used for the ranking of the cWB events. To be robust against the non-stationary detector noise, cWB employs signal independent vetoes, which reduce the high rate of the initial excess power triggers. The cWB primary veto cut is on the network correlation coefficient $\mathrm{cc} = E_C/(E_C + E_N)$ where E_N is the residual noise energy estimated after the reconstructed signal is subtracted from the data [13]. Typically, for a GW signal $\mathrm{cc} \approx 1$ and for instrumental glitches $\mathrm{cc} \ll 1$. Therefore, during the last observing runs by the advanced GW detectors, events with $\mathrm{cc} < 0.7$ were rejected as potential glitches. Finally, cWB can extend its capabilities by using linear combinations of wavelets basis functions providing an overcomplete decomposition of the signal, the so-called *patterns*. In order to improve the detection efficiency for stellar mass BBH sources, cWB adopted a pattern favouring those events for which the frequency is increasing with time, i.e. events with a chirping time-frequency. Such a time-frequency pattern captures the phenomenological behavior of most CBC sources. This loose constraint allows cWB to potentially identify CBC sources with features such as higher order modes, high mass ratios, misaligned spins and eccentric orbits, then complementing the existing templated algorithms by searching for new and possibly unexpected CBC populations.

All results reported in this paper have been produced by the open source version 6.3.0 of cWB: this version has been publicly released for open use and it reproduces cWB scientific results included in the most recent publications of the LIGO-Virgo collaboration based on the observing runs 1 and 2. The pipeline and production parameters are the same as in the abovementioned publications with minimal changes in the code to enable measurement of quantities needed for the Monte Carlo. While cWB can work with arbitrary detector networks, the waveform reconstruction has been restricted to the Hanford and Livingston detectors, due to the small contribution by Virgo data to the morphological reconstruction of the events; Virgo data was indeed used (when available) for the sky localization results reported in Table III.

B. Monte Carlo simulation methodology

While the unmodeled sky localization and waveform reconstruction by cWB are usually in agreement with the current modeled parameter estimations [1], some discrepancies occasionally arise mostly due to the lack of strong constraints on the waveform. We have devised a new methodology based on Monte Carlo simulations to estimate the reconstruction uncertainties: results produced with this technique are shown on section IV on [1]. Similarly, in this paper, we make use of the public parameter estimation samples by LALInference [14] released for GWTC-1 to set-up a Monte Carlo simulation: for each GW event, we add to real data thousands of waveforms from the corresponding reference sample of parameter estimation posteriors at random times (in a time span close to the event); next, for each such injection we perform an unmodeled reconstruction and determine the maximum likelihood point-like estimated waveform and the full likelihood sky map; the ensemble of those build empirical distributions of cWB waveform reconstructions which are marginalized with respect to the adopted posterior reference samples (in this case, with respect to LALInference parameter estimations) and which includes all effects due to non-Gaussian noise fluctuations as well as all biases due to cWB estimation itself. These rich distributions of waveform and sky localization reconstructions allow the estimation of waveform frequentist confidence intervals

public repositories, `https://gitlab.com/gwburst/public` documentation, `https://gwburst.gitlab.io/documentation/latest/html/index.html`.

[2] The LIGO-Virgo data are publicly available at the Gravitational Wave Open Science Center [10]; the LIGO-Virgo release of waveform posterior samples is at `https://dcc.ligo.org/LIGO-P1800370/public`.

and the likelihood sky map coverage. For more details on the actual implementation of the Monte Carlo, please refer to Appendix B.

III. RESULTS

The Advanced LIGO [2] detectors started taking data on September 12^{th}, 2015 until January 19^{th}, 2016. This run is referred to as O1. The Advanced LIGO detectors started their second run, called O2, on November 30^{th}, 2016; on the first of August, 2017 the Advanced Virgo [3] detector joined the observing run, enabling the first three-detector observations of GWs. This second run ended on August 25^{th}, 2017. During the first and the second runs, the LIGO-Virgo searches for binary mergers (both those with matched filters and unmodeled) identified a total of ten BBH mergers and one binary neutron star (BNS) signal. All relevant information on those GW events can be found on the Gravitational-Wave Transient Catalog of Compact Binary Mergers (GWTC−1) [1] and on a number of other papers dedicated to individual GW events [15–20]. Moreover, information on O1 GW events including a large set of subthreshold candidates can be found in [21]. Finally, previous tests checking for deviations from CBC models have been discussed in [4].

When considering cWB reconstruction of the eleven main events from the GWTC−1, a subset (i.e. GW151012, GW151226, GW170729, GW170809 and GW170814) shows some features in well-localized regions of the time-frequency representation which are missing in the usual CBC waveforms, mainly close to the merger time (see Figure 1, Figures 3 (a) and (d) and Figures 5 (a) and (d)).

A. cWB unmodeled reconstruction of the events within GWTC–1

For each GW event, we compared the cWB sky localization likelihood map with the corresponding posterior probability sky regions produced by LALInference [14]: while the unmodeled reconstruction produces larger sky regions and different biases may arise [3], especially for two-detector networks, the overall overlap between the estimates by cWB and LALInference is mostly good. More details can be found in appendix A, in particular in Table III and in Figure 7.

Similarly, for each GW event, the waveforms reconstructed by cWB were compared with those reconstructed from the Monte Carlo which uses LALInference posterior samples: as expected from an algorithm based on excess power, the merger part of the signal is usually well estimated by cWB, while the early inspiral and the ringdown parts (where the signals are weaker and spread over larger area in the time-frequency plane) are often missing.

Starting from the CBC modeled strain waveforms at the Hanford and Livingston sites, $\mathbf{h} = [h_H(t), h_L(t)]$ and the cWB estimated noise spectral densities, we define the corresponding CBC whitened waveforms, $\mathbf{w} = [w_H(t), w_L(t)]$; by denoting the model-independent whitened cWB waveforms as $\hat{\mathbf{w}}$, we can calculate the generalized fitting factor of $\hat{\mathbf{w}}$ with respect to $\mathbf{w}$ as

$$\mathrm{FF}(\mathbf{w}, \hat{\mathbf{w}}) = \frac{(\mathbf{w}|\hat{\mathbf{w}})}{\sqrt{(\mathbf{w}|\mathbf{w})}\sqrt{(\hat{\mathbf{w}}|\hat{\mathbf{w}})}} \tag{1}$$

where the scalar product is defined in the time domain as

$$(\mathbf{x}|\mathbf{y}) = \int_{\mathbf{t_1}}^{\mathbf{t_{coa}}} \mathbf{x}(t)\mathbf{y}(t)dt \tag{2}$$

with $\mathbf{t}_1 = [t_{H,1}, t_{L,1}]$ defined as $\int_{-\infty}^{\mathbf{t}_1} |\mathbf{x}(t)|^2 dt = 0.01 \int_{-\infty}^{\infty} |\mathbf{y}(t)|^2 dt$ and $\mathbf{t_{coa}} = [\mathrm{t_{H,coa}}, \mathrm{t_{L,coa}}]$ is the coalescence time [4].

In Table I, we report the average $\langle \mathrm{FF} \rangle_{\mathrm{offsource}}$ calculated by Monte Carlo sampling, where for each injected LALInference posterior, $\mathbf{h}^i(t)$ (the index i runs over all posterior samples; see Appendix II B for more details) we calculate $\mathrm{FF}(\mathbf{w}^i(t), \hat{\mathbf{w}}^i(t))$, as well as the "onsource" average FF, i.e. $\langle \mathrm{FF} \rangle_{\mathrm{onsource}} = \langle \mathrm{FF}(\mathbf{w}^i(t), \hat{\mathbf{w}}^{\mathrm{gw}}(t)) \rangle_i$, where $\hat{\mathbf{w}}^{\mathrm{gw}}(t)$ is the actual cWB whitened waveform of the GW event.

By defining the residual energy of $\hat{\mathbf{w}}^{\mathrm{gw}}$ with respect to i^{th} CBC whitened sample $\mathbf{w}^i$ as

$$\mathbf{E}^i_{\mathrm{res}} = \int_{\mathbf{t}^i_A}^{\mathbf{t}^i_B} \left| \mathbf{w}^i(t) - \hat{\mathbf{w}}^{\mathrm{gw}}(t) \right|^2 dt \tag{3}$$

with $\mathbf{t}_{A,B}$ defined as $\int_{-\infty}^{\mathbf{t}_A} |\hat{\mathbf{w}}^{gw}(t)|^2 dt = \int_{\mathbf{t}_B}^{\infty} |\hat{\mathbf{w}}^{gw}(t)|^2 dt = 0.02 \int_{-\infty}^{\infty} |\hat{\mathbf{w}}^{gw}(t)|^2 dt$, we can then calculate the sample i corresponding to $\min_i \left(\left| \left| \mathbf{E}^i_{\mathrm{res}} \right| \right| \right)$ and denote it as the minimal residual energy posterior sample, minR.

The relatively high $\langle \mathrm{FF} \rangle_{\mathrm{offsource}}$ suggests that there is a good agreement between the modeled and the unmodeled waveform reconstruction before coalescence time. Moreover, from the comparison of the onsource and offsource FFs, we can infer a qualitative compatibility between estimates, with the exception of GW170809, which we shall investigate further in the future.

[3] cWB customarily employs an antenna pattern prior, which overweights favorable incoming directions, while underweighting the ones with poor antenna pattern.

[4] In this article, we considered just the IMRPhenomP waveform family, where the $\mathrm{t_{coa}}$ is the estimated time (with a stationary phase approximation) corresponding to the $\mathrm{f_{peak}}$ as defined in Eq. 20 in [7].

B. Significance of post-coalescence excesses

A number of cWB excesses with respect to the CBC templates occur after the coalescence, where CBC waveforms are mostly silent. In order to estimate their significance, we devised a procedure based on their coherent network SNR. We considered the coalescence time, i.e. $t_{\rm coa}$, as a reference time to start integrating our excesses: we then split our reconstructed waveforms in a *primary* part (i.e. for $t \leq t_{\rm coa}$) and a *secondary* part (i.e. for $t > t_{\rm coa}$). Our main test-statistic is then

$$\mathrm{SNR}_{\rm pc} = \sqrt{\int_{\mathbf{t}_{\rm coa}}^{\infty} |\hat{\mathbf{w}}(t)|^2 \, dt} \qquad (4)$$

[5]. While for the offsource Monte Carlo simulations, the $t_{\rm coa}$ are known from the CBC posterior samples, for the onsource the $t_{\rm coa}$ can only be estimated, leaving a margin for uncertainty on the onsource SNR_{pc}. We decided to adopt $t_{\rm coa}^{\rm minR}$, i.e. the coalescence time of the minimal residual energy CBC posterior sample (already defined in Section III A) as our best point estimate. On TableI, we report the $\mathrm{SNR}_{\rm pc}^{\rm minR}$, together with the upper and lower bounds, $\mathrm{SNR}_{\rm pc}^{\rm sup}$ and $\mathrm{SNR}_{\rm pc}^{\rm inf}$ which correspond to $\langle \mathrm{t_{coa}} \rangle \pm 2\ \sigma$. Finally, in the last column of Table I, we report the estimated p-value for the onsource coherent SNR excess as the ratio of the number of offsource reconstructed waveforms with a larger or equal value of coherent $\mathrm{SNR}_{\rm pc}$ over the total number of Monte Carlo reconstructed injections. Consistently with the definition of 2σ SNR upper and lower bounds, we reported the upper and lower bounds for the p-value. In order to evaluate the result in the context of multiple hypothesis tests, i.e. when comparing many data against a given hypothesis, we considered the false-discovery rate (FDR) procedure to control the number of mistakes made when selecting potential deviations from the null hypothesis [22]: the result is shown in Figure 2 where the sorted post-coalescence p-values (black dots represent the minR p-values, while the blue and light green vertical lines show the 1 and 2 σ [$P_{\rm sup}$-$P_{\rm inf}$] bounds, respectively) are plotted against the ranking probability (rank/$N_{\rm events}$) and compared with an FDR light green dashed area (with false alarm probability $\alpha = 0.1$). Out of the 11 GW events, the post-coalescence p-value$_{\rm pc}$ for GW151012 is an outlier. The second ranked event, GW151226, though mildly significant is consistent with the 11 trials.

C. Follow-ups on GW151012 and GW151226

The original reconstruction of GW151012 reveals a primary part consistent with the time-frequency evolution estimated by LALInference, followed by a secondary part, with a chirping structure, at roughly 200 ms after the merger of GW151012, as shown on Figure 3 (a). The E_N on Figure 3 (d) shows that the secondary part, when reconstructed together with the primary, has some relatively high residuals. In order to produce the plots on the second and third columns of Figure 3, we applied ad-hoc time vetoes to reconstruct indipendently the primary (b and e) and secondary ((c) and (f)). As we see from Figure 4 (a), the estimated sky localizations substantially differ between the primary (blue) and the secondary (green), when reconstructed independently. The main reason being the reconstructed time delay between the detectors (Figure 4 (b)). This is a hint that the primary and secondary are not related to one another.

A similar follow-up analysis was conducted also on GW151226. On Figure 5 (a) and (d) the secondary is visible at roughtly 100 ms. The plots on the second and third columns of Figure 5, show the primary (b and e) and secondary ((c) and (f)) reconstructed indipendently of one another; the latter being very weak and lacking any structure. Figures 6 (a) and (b) show that the estimated sky localizations of the primary (blue) and the secondary (green) could be compatible.

The follow-up parameters for GW151012 and GW151226 are reported on Table II, where the network SNR, the correlation coefficient (defined in Section II A) and the chirp mass as estimated by LALInference (PE) and by cWB [23] in the original reconstruction and by isolating the primary and the secondary can be found. When comparing the network SNRs of the primary with the estimates by LALInference, we find an SNR loss of $\approx$ 10–15%; cWB chirp mass estimates are mostly used just as an indication of "chirpness" as its estimator relies on simplified assumptions that can lead to relatively large biases.

IV. DISCUSSION

In this paragraph we focus on the two outliers of the distribution of post coalescence features from Table I, GW151012 and GW151226. The p-values are too large to exclude the null hypothesis, and yet it is useful to consider alternative explanations to exemplify the kind of findings that could be borne out of our methodology. To further stress this point, we remark that we also extended the duration of the post-coalescence analysis of GW150914 and GW170817, obtaining results that in both cases agree with the null hypothesis.

A. GW151012

A first plausible interpretation for the primary and secondary features in the cWB reconstruction of GW151012 is that it may consist of an accidental coincidence of unrelated CBC events of different chirp masses and direc-

[5] The resulting $\mathrm{SNR}_{\rm pc}$ of the *secondary* will then include a small fraction of the primary signal, i.e. the ringdown.

GW event	**source**	$\langle \mathrm{FF} \rangle_{\mathrm{offsource}}$	$\langle \mathrm{FF} \rangle_{\mathrm{onsource}}$	$\mathrm{FF}^{\mathrm{minR}}$	SNR	$\mathrm{SNR}_{\mathrm{pc}}^{\mathrm{minR}} \left\{ {}^{\mathrm{SNR}_{\mathrm{pc}}^{\mathrm{sup}}}_{\mathrm{SNR}_{\mathrm{pc}}^{\mathrm{inf}}} \right\}$	$\text{p-value}_{\mathrm{pc}} \left\{ {}^{P_{\mathrm{sup}}}_{P_{\mathrm{inf}}} \right\}$
GW150914	BBH	0.95 ± 0.02	0.96 ± 0.01	0.97	25.2	$5.72\ {}^{6.92}_{5.64}$	$0.94 \pm 0.02\ {}^{0.95}_{0.71}$
GW151012	BBH	0.80 ± 0.10	0.82 ± 0.038	0.9	10.5	$6.60\ {}^{6.54}_{6.26}$	$0.0037 \pm 0.0014\ {}^{0.0068}_{0.0042}$
GW151226	BBH	0.78 ± 0.08	0.75 ± 0.05	0.85	11.9	$4.40\ {}^{4.41}_{4.36}$	$0.025 \pm 0.005\ {}^{0.03}_{0.02}$
GW170104	BBH	0.90 ± 0.05	0.95 ± 0.03	0.97	13.0	$5.29\ {}^{5.30}_{3.95}$	$0.07 \pm 0.01\ {}^{0.31}_{0.07}$
GW170608	BBH	0.79 ± 0.07	0.81 ± 0.02	0.84	14.1	$1.69\ {}^{1.75}_{1.64}$	$0.51 \pm 0.02\ {}^{0.54}_{0.49}$
GW170729	BBH	0.90 ± 0.05	0.93 ± 0.02	0.95	10.2	$4.81\ {}^{4.86}_{3.43}$	$0.09 \pm 0.01\ {}^{0.35}_{0.08}$
GW170809	BBH	0.90 ± 0.04	0.78 ± 0.03	0.82	11.9	$3.89\ {}^{4.71}_{3.88}$	$0.28 \pm 0.01\ {}^{0.28}_{0.11}$
GW170814	BBH	0.92 ± 0.03	0.91 ± 0.02	0.93	17.2	$5.98\ {}^{6.02}_{5.94}$	$0.10 \pm 0.01\ {}^{0.11}_{0.09}$
GW170817	BNS	0.78 ± 0.05	0.7596 ± 0.0004	0.76	29.3	$0.21\ {}^{0.21}_{0.21}$	$0.55 \pm 0.01\ {}^{0.56}_{0.55}$
GW170818	BBH	0.89 ± 0.06	0.87 ± 0.01	0.92	8.6	$1.97\ {}^{2.04}_{1.76}$	$0.87 \pm 0.02\ {}^{0.91}_{0.86}$
GW170823	BBH	0.91 ± 0.05	0.96 ± 0.03	0.98	10.8	$3.11\ {}^{3.54}_{2.69}$	$0.60 \pm 0.02\ {}^{0.74}_{0.44}$

TABLE I. Significance of post-coalescence deviations recostructed by cWB on the eleven GW events from GWTC-1: for each event we report offsource and onsource average fitting factors, FF, with 1 σ uncertainties, the onsource FF corresponding to the minimal residual energy posterior sample, the network SNR as estimated by cWB, the post-coalescence SNR, $\mathrm{SNR}_{\mathrm{pc}}^{\mathrm{minR}}$, assuming the t_{coa} from the minR posterior sample (while $\mathrm{SNR}_{\mathrm{pc}}^{\mathrm{sup}}$ and $\mathrm{SNR}_{\mathrm{pc}}^{\mathrm{inf}}$ are the onsource $\mathrm{SNR}_{\mathrm{pc}}$ corresponding to $\langle \mathrm{t_{coa}} \rangle$ $\pm 2\sigma$, respectively) and, finally, the empirically estimated probability that such an $\mathrm{SNR}_{\mathrm{pc}}^{\mathrm{minR}}$ may be produced by a noise fluctuation (where the P_{sup} and P_{inf} values refer to the probability of $\mathrm{SNR}_{\mathrm{pc}}^{\mathrm{inf}}$ and $\mathrm{SNR}_{\mathrm{pc}}^{\mathrm{sup}}$, respectively).

GW event	SNR				cc			Chirp Mass [$\mathrm{M}_{\odot}$]			
	PE	original	primary	secondary	original	primary	secondary	PE	original	primary	secondary
GW151012	10.0	10.5	8.4	7.1	0.81	0.95	0.83	15.2	23.8	23.8	3.2
GW151226	13.1	11.9	11.4	4.0	0.82	0.85	0.86	8.9	10.4	10.4	—

TABLE II. Follow-up parameters for GW151012 and GW151226: the network SNR, the correlation coefficient (defined in Section II A) and the chirp mass as estimated by LALInference (PE) and by cWB in the original reconstruction and by isolating the primary and the secondary.

tion, compatible with catalogs of subthreshold CBC candidates, see in particular 1-OGC [21]. While the primary component is a well established CBC detection, the secondary feature on its own is much fainter and its probability of being originated by coherent noise from the detectors is close to one. In any case, even assuming an astrophysical origin for the secondary, according to our morphological analysis the two GWs would be unrelated.

The secondary feature shows traits which are consistent with the CBC subthreshold candidates in the 1-OGC catalog [21], both morphologically and in terms of signal amplitude. In fact, its morphology is consistent with a coalescence of a light stellar mass binary, within the parameter space included by the template bank of the 1-OGC search. Also the SNR values collected at each detector by cWB are larger than 4, the threshold used for 1-OGC, and the network SNR recovered by cWB is very close to the mode of the SNR distribution of the subthreshold events in 1-OGC. [6] We expect that the SNR collected by cWB be statistically comparable with the one collected by CBC matched filter searches. This is tested for the detections described in the GWTC-1 catalog [1], and we expect it to hold also at the fainter amplitudes comparable to the secondary. The secondary feature was not found in 1-OGC search for subthresholds CBC candidates because of the dead time set around all reconstructed events, such as the primary [21].

The rate of occurrence of subthreshold CBC candidates in 1-OGC is ~ 0.06 Hz, estimated from the total counts of candidates divided by the net observation time after accounting for the deadtime around each selected candidate. cWB clusters together two signals if their time separation is less than 0.2 s, which corresponds to

[6] The secondary feature calls for a mass ratio of the binary component significantly different from 1, from simplified matched filter analyses

opening a time window of variable width after the coalescence time, depending on the actual duration of each signal component. In the case of GW151012, the typical time window ranges from 0.25 s for faint BBH-like secondaries to 0.37 s for faint BNS-like secondary. Therefore, the probability of random occurrence after coalescence of a subthreshold 1-OGC event within the cWB window ranges from 1.4% to 2.1% during the O1 run. Assuming similar rates for the subthreshold events in the O2 run, the order of magnitude of this probability is high enough to allow the possible occurrence of a CBC-like secondary in one out of the 11 regions after coalescence tested here. On the other hand, this probability is low enough not to be inconsistent with the measured p-value of GW151012, taking into account the uncertainties on the detection efficiency loss of cWB for candidates of the class of the 1-OGC candidates after the primary coalescence. Therefore we conclude that the secondary feature has a plausible interpretation as an object of the class of the subthreshold CBC candidates, which in turn have a population dominated by coherent noise fluctuations.

Our morphological analysis strongly disfavors any interpretation of the post-coalescence feature that is directly related to the detected GW151012, because of the inconsistency in the delay times at the detectors, which call for a different source position. In particular, this analysis disfavors alternative interpretations as post-merger echoes (see previous analyses in [25] and [26]), despite an apparent agreement in the delay time from merger and amplitude. In addition, the spectral content we reconstruct does not fit the proposed echoes models.

B. GW151226

The p-value of the post-coalescence feature is only marginally interesting in our analysis, and the preferred interpretation is the null hypothesis. Here, the alternative, though statistically disfavored, interpretation for the post-coalescence feature – a single tone at ~ 160 Hz with total duration ~ 0.03 s delayed by ~ 0.1 s – could be a fainter repetition of the merger. This would not be in contradiction with e.g. microlensing of the GW primary or GW echoes. Microlensing could explain the observed delay time, corresponding to a fractional travel time of $\sim 2 \times 10^{-18}$, though it would require characteristics and position of the lens which appear highly unlikely from back of the envelope estimations, further favoring the simpler null hypothesis. Our result also does not support echoes with respect to the null hypothesis, in agreement with previous targeted searches analyzing GW151226 and specifically aimed at echoes (see e.g. [25–28]).

C. other GWTC-1 GWs

The standard cWB analysis of all other GWTC-1 events does not show any significant deviation from the null hypothesis in the post-coalescence tests, as reported in Table I. However, our standard setting constrains signal clustering to a time-window smaller than $\sim$ 0.3 s, which is not sufficient to capture the echoes-signal claimed for GW150914 and GW170817 by [25, 29]. Motivated by their findings, we decided to expand up to 5 s the on-source time-window allowed for signal clustering in the cWB analysis. In the case of GW150914, this extension results in the appearance of an on source post-merger with null coherent SNR and non zero incoherent energy, therefore we can conclude that there is no support for any signal coming from a direction consistent with GW150914. In the case of GW170817, this extension shows a short burst of ~ 0.01 s duration and frequency ~ 130 Hz at a delay of ~ 1 s with coherent and incoherent components. By repeating the same experiment off-source, the p-value of the coherent on source SNR in the post-coalescence is about 20%, which confirms the null hypothesis. The morphology of the cWB feature is compatible with the first harmonic of the signal claimed by [29], however, when compared with the widest class of possible post-merger events, as we do here, its p-value becomes uninteresting. These results, however, are not sufficient to invalidate nor confirm the echoes model of [29]: in fact, to be able to compare quantitatively the sensitivity of this analysis with the template searches for echoes, we would need to calibrate the detection efficiency of the cWB analysis for that specific signal class, which is beyond the scope of the present paper.

V. CONCLUSIONS

The CBC waveforms used in PyCBC, GstLAL and other similar pipelines [10], are the result of sophisticated calculations with a well-defined set of physical assumptions. The methodology discussed in this work is aimed at complementing the template based pipelines and detecting additional features that may show up in the observed time-frequency data as localized excesses of coherent SNR across the network. Indeed, any significant excess coherent energy can indicate the presence of astrophysical structures that reshape the theoretical waveform or point to some still unobserved physics.

Our analysis of the events in the GWTC-1 catalog [1] identifies distinct features after coalescence in the events GW151012 and GW151226 with a statistical significance which is insufficient to make any claim about their astrophysical origin, but that calls for further investigations. On one side we studied the morphology of these features to search for plausible explanations, alternative to the null hypothesis. On the other side, we look forward to

apply this analysis to the larger set of upcoming compact binary coalescences which will be detected in the current observation run of LIGO-Virgo.

In the case of GW151012, the secondary feature is consistent with a subthreshold candidate of a compact binary coalescence. Both its apparent chirpmass and apparent sky direction are different from those of the primary CBC GW signal, which seems to indicate that the secondary is unrelated to the primary and may plausibly be due to the accidental coincidence with a subthreshold CBC candidate with the primary event. If this interpretation is correct, the higher sensitivity of the interferometers in the O3 observing run should lead to several more such observations.

In the case of GW151226, the morphology of the feature that appears after coalescence may suggest a post-merger phenomenon related to the detected GW, also in view of the near superposition of skymap distributions. Again, we interpret this as a simple noise fluctuation. However, it will be interesting to repeat the analysis on the larger set of GWs from the current observation run and check how frequently this type of outliers occurs.

We conclude by remarking that we have established a new general methodology in the framework of cWB, that can be extended to search for a larger variety of additional features, not currently included in the CBC models. In the future, we plan to widen our statistical tests to other regions of the time-frequency representation and to appraise the sensitivity of the analysis for selected models of astrophysical phenomena.

Appendix A: cWB sky localizations for GW events within GWTC−1

The reconstructed sky locations of the gravitational wave events estimated by cWB are reported in Figure 7. Plots show the 10%, 50% and 90% credible regions comparing the results from cWB (blue) and LALInference (red). For 5 events the inclusion of Virgo detector naturally reduces the overall area of credible region for both algorithms. In Table III, we report the values of 50% and 90% credible regions for cWB and LALInference, together with the extension of the overlapping area between the two estimations. The last two columns report the nominal probability estimated by the two algorithms when we restrict the integration inside this overlap area. Generally the results show that there is a dominant overlap when only two detectors are considered, while the modeled reconstruction is considerably reduced with respect to the unmodeled one when Virgo is added in the network.

Appendix B: Posteriors injection simulation

The implemented Monte Carlo methodology allows for the injection of waveform models from the public parameter estimation samples released for GWTC-1 events: those samples have been injected every 150 s in the O1-O2 data around the GW event considered (i.e. corresponding roughly to five days of interferometers coincident time including the GW triggers) with the aim of achieving at least one thousand reconstructions for each GW event. For the BBH systems this procedure employs the IMRPhenomPv2 waveform family [30–32], a phenomenological waveform family that models signal from the inspiral, merger, ringdown phase taking in to account spin effects, and including simple precession, whereas effects of subdominant (non-quadrupole) mode are not included. For the BNS system the model IMRPhenomPv2_NRTidal is considered [33], [34], it includes numerical relativity (NR)-tuned tidal effects, the spin-induced quadrupole moment.

The cWB unmodelled algorithm is applied to recover the injections, using the same setting of parameters used for O2 analysis, including the veto due to the quality of the data. All the point estimated reconstructions are used to build empirical distribution of reconstructed signals. This methodology allows to obtain a marginalization over the posterior distribution of the models and to estimate possible bias due to non Gaussian noise fluctuations, of the data in the time period of the event.

ACKNOWLEDGMENTS

The authors would like to thank Ik Siong Heng for his constructive inputs. We also acknowledge useful discussions with Marco Cavaglia, Tom Dent, Sudarshan Ghonge and Tyson Littenberg. This research has made use of data, software and/or web tools obtained from the Gravitational Wave Open Science Center (https://www.gw-openscience.org), a service of LIGO Laboratory, the LIGO Scientific Collaboration and the Virgo Collaboration. The work by S.Tiwari was supported by SNSF grant #200020_182047. Finally, we gratefully acknowledge the support of the State of Niedersachsen/Germany and NSF for provision of computational resources.

[1] Abbott, B. P. and others (LIGO Scientific Collaboration and Virgo Collaboration), GWTC-1: A Gravitational-Wave Transient Catalog of Compact Binary Mergers Observed by LIGO and Virgo during the First and Second Observing Runs (2018), arXiv:1811.12907.

[2] J. Aasi and others (LIGO Scientific Collaboration), Advanced LIGO (2015).

[3] F. Acernese and others (Virgo Collaboration), Advanced

GW event	**source**	**network**	**CR**	Sky area [deg^2]			P(Overlap)	
				cWB	CBC	Overlap	cWB	CBC
GW150914	BBH	HL	50%	135.1	52.0	5.0	0.043	0.013
			90%	446.9	176.0	109.9	0.640	0.226
GW151012	BBH	HL	50%	627.8	437.5	285.2	0.351	0.223
			90%	2195.4	1509.7	1412.7	0.882	0.648
GW151226	BBH	HL	50%	419.4	343.3	184.9	0.267	0.218
			90%	1393.9	1046.4	902.0	0.841	0.659
GW170104	BBH	HL	50%	437.1	205.8	144.1	0.370	0.191
			90%	1398.7	939.0	711.7	0.783	0.612
GW170608	BBH	HL	50%	285.6	95.5	25.0	0.098	0.039
			90%	1067.0	375.4	331.9	0.833	0.463
GW170729	BBH	HLV	50%	296.5	145.6	84.8	0.232	0.148
			90%	1476.5	1049.5	870.6	0.842	0.716
GW170809	BBH	HLV	50%	298.4	73.4	55.6	0.403	0.088
			90%	1747.4	344.5	246.1	0.787	0.268
GW170814	BBH	HLV	50%	77.0	18.0	6.9	0.183	0.032
			90%	672.1	98.4	89.8	0.863	0.434
GW170817	BNS	HLV	50%	548.7	5.5	1.0	0.089	0.001
			90%	1965.6	19.7	19.9	0.901	0.010
GW170818	BBH	HLV	50%	95.7	8.8	—	—	—
			90%	1707.5	32.1	14.5	0.405	0.005
GW170823	BBH	HL	50%	532.3	457.4	424.3	0.475	0.417
			90%	1634.3	1795.9	1489.1	0.851	0.871

TABLE III. For each of the GW events, we report a comparison between cWB and LALInference (CBC) reconstructed sky localizations: 50% and 90% sky areas with their ovelap are reported. In the last two columns, we give the nominal probability as estimated by cWB and LALInference integrated over the overlap area. For 5 GW events, i.e. GW170729, GW170809, GW170814, GW170817 and GW170818, the localizations can benefit from the data from a third site, i.e. Virgo.

Virgo: a second-generation interferometric gravitational wave detector (2015).

[4] Abbott, B. P. and others (LIGO Scientific Collaboration and Virgo Collaboration), Tests of General Relativity with the Binary Black Hole Signals from the LIGO-Virgo Catalog GWTC-1 (2019), arXiv:1903.04467.

[5] C. M. Biwer, C. D. Capano, S. De, M. Cabero, D. A. Brown, A. H. Nitz, and V. Raymond, PyCBC Inference: A Python-based Parameter Estimation Toolkit for Compact Binary Coalescence Signals, Publications of the Astronomical Society of the Pacific **131**, 024503 (2019).

[6] C. Cutler, The last three minutes: Issues in gravitational-wave measurements of coalescing compact binaries, Physical Review Letters **70**, 2984 (1993).

[7] S. Khan, S. Husa, M. Hannam, F. Ohme, M. Pürrer, X. J. Forteza, and A. Bohè, Frequency-domain gravitational waves from nonprecessing black-hole binaries. II. A phenomenological model for the advanced detector era, Physical Review D **93**, 10.1103/PhysRevD.93.044007 (2016).

[8] S. Khan, K. Chatziioannou, M. Hannam, and F. Ohme, Phenomenological model for the gravitational-wave signal from precessing binary black holes with two-spin effects (2018), arXiv:1809.10113 [gr-qc].

[9] J. Calderón Bustillo, F. Salemi, T. Dal Canton, and K. P. Jani, Sensitivity of gravitational wave searches to the full signal of intermediate-mass black hole binaries during the first observing run of Advanced LIGO, Phys. Rev. D **97**, 024016 (2018).

[10] Gravitational Wave Open Science Center, https://www.gw-openscience.org/software/.

[11] B. P. Abbott *et al.* (KAGRA, LIGO, VIRGO), Prospects for Observing and Localizing Gravitational-Wave Transients with Advanced LIGO, Advanced Virgo and KAGRA, Living Rev. Rel. **21**, 3 (2018), arXiv:1304.0670 [gr-qc].

[12] S. Klimenko *et al.*, Method for detection and reconstruction of gravitational wave transients with networks of advanced detectors, Phys. Rev. D **93**, 042004 (2016), arXiv:1511.05999 [gr-qc].

[13] S. Klimenko, I. Yakushin, A. Mercer, and G. Mitselmakher, Coherent method for detection of gravitational wave bursts, Class. Quantum Grav. **25**, 114029 (2008), arXiv:0802.3232.

[14] J. Veitch *et al.*, Parameter estimation for compact binaries with ground-based gravitational-wave observations using the LALInference software library, Phys. Rev. **D91**, 042003 (2015), arXiv:1409.7215 [gr-qc].

[15] B. P. Abbott *et al.*, Observation of Gravitational Waves from a Binary Black Hole Merger, Phys.Rev.Lett. **116**, 061102 (2016), LIGO-P150914.

[16] B. P. Abbott *et al.*, GW151226: Observation of Gravitational Waves from a 22-Solar-Mass Binary Black Hole Coalescence , Phys.Rev.Lett. **116**, 241103 (2016), LIGO-P151226.

[17] B. P. Abbott *et al.* (Virgo Collaboration, LIGO Scientific Collaboration), GW170104: Observation of a 50-Solar-Mass Binary Black Hole Coalescence at Redshift 0.2, Phys. Rev. Lett. **118**, 221101 (2017), arXiv:1706.01812 [gr-qc].

[18] B. P. Abbott *et al.* (Virgo Collaboration, LIGO Scientific Collaboration), GW170608: Observation of a 19-solar-mass Binary Black Hole Coalescence, Astrophys. J. **851**, L35 (2017), arXiv:1711.05578 [astro-ph.HE].

[19] B. P. Abbott *et al.* (Virgo Collaboration, LIGO Scientific Collaboration), GW170814: A Three-Detector Observation of Gravitational Waves from a Binary Black Hole Coalescence, Phys. Rev. Lett. **119**, 141101 (2017), arXiv:1709.09660 [gr-qc].

[20] B. P. Abbott *et al.* (LIGO Scientific Collaboration and Virgo Collaboration), GW170817: Observation of Gravitational Waves from a Binary Neutron Star Inspiral, Phys. Rev. Lett. **119**, 161101 (2017).

[21] A. H. Nitz, C. Capano, A. B. Nielsen, S. Reyes, R. White, D. A. Brown, and B. Krishnan, 1-OGC: The first open gravitational-wave catalog of binary mergers from analysis of public advanced LIGO data, The Astrophysical Journal **872**, 195 (2019).

[22] C. J. Miller, C. Genovese, R. C. Nichol, L. Wasserman, A. Connolly, D. Reichart, A. Hopkins, J. Schneider, and A. Moore, Controlling the false-discovery rate in astrophysical data analysis, The Astronomical Journal **122**, 3492 (2001).

[23] V. Tiwari, S. Klimenko, V. Necula, and G. Mitselmakher, Reconstruction of chirp mass in searches for gravitational wave transients, Classical and Quantum Gravity **33**, 01LT01 (2015).

[24] R. Essick, skymap_statistics, https://github.com/reedessick/skymap_statistics, Free software (GPL).

[25] J. Abedi, H. Dykaar, and N. Afshordi, Echoes from the Abyss: Tentative evidence for Planck-scale structure at black hole horizons, Physical Review D **96**, 082004 (2017).

[26] A. B. Nielsen, C. D. Capano, and J. Westerweck, Parameter estimation for black hole echo signals and their statistical significance, arXiv preprint arXiv:1811.04904 (2018).

[27] G. Ashton, O. Birnholtz, M. Cabero, C. Capano, T. Dent, B. Krishnan, G. D. Meadors, A. B. Nielsen, A. Nitz, and J. Westerweck, Comments on:"Echoes from the abyss: Evidence for Planck-scale structure at black hole horizons", arXiv preprint arXiv:1612.05625 (2016).

[28] J. Westerweck, A. B. Nielsen, O. Fischer-Birnholtz, M. Cabero, C. Capano, T. Dent, B. Krishnan, G. Meadors, and A. H. Nitz, Low significance of evidence for black hole echoes in gravitational wave data, Physical Review D **97**, 124037 (2018).

[29] J. Abedi and N. Afshordi, Echoes from the Abyss: A highly spinning black hole remnant for the binary neutron star merger GW170817, arXiv preprint arXiv:1803.10454 (2018).

[30] S. Husa, S. Khan, M. Hannam, M. Pürrer, F. Ohme, X. J. Forteza, and A. Bohé, Frequency-domain gravitational waves from nonprecessing black-hole binaries. I. New numerical waveforms and anatomy of the signal, Phys. Rev. D **93**, 044006 (2016).

[31] M. Hannam, P. Schmidt, A. Bohé, L. Haegel, S. Husa, F. Ohme, G. Pratten, and M. Pürrer, Simple Model of Complete Precessing Black-Hole-Binary Gravitational Waveforms, Phys. Rev. Lett. **113**, 151101 (2014).

[32] P. Schmidt, F. Ohme, and M. Hannam, Towards models of gravitational waveforms from generic binaries II: Modelling precession effects with a single effective precession parameter, Phys. Rev. **D91**, 024043 (2015), arXiv:1408.1810 [gr-qc].

[33] T. Dietrich, S. Bernuzzi, and W. Tichy, Closed-form tidal approximants for binary neutron star gravitational waveforms constructed from high-resolution numerical relativity simulations, Phys. Rev. D **96**, 121501 (2017).

[34] T. Dietrich, S. Khan, R. Dudi, S. J. Kapadia, P. Kumar, A. Nagar, F. Ohme, F. Pannarale, A. Samajdar, S. Bernuzzi, G. Carullo, W. Del Pozzo, M. Haney, C. Markakis, M. Pürrer, G. Riemenschneider, Y. E. Setyawati, K. W. Tsang, and C. Van Den Broeck, Matter imprints in waveform models for neutron star binaries: Tidal and self-spin effects, Phys. Rev. D **99**, 024029 (2019).

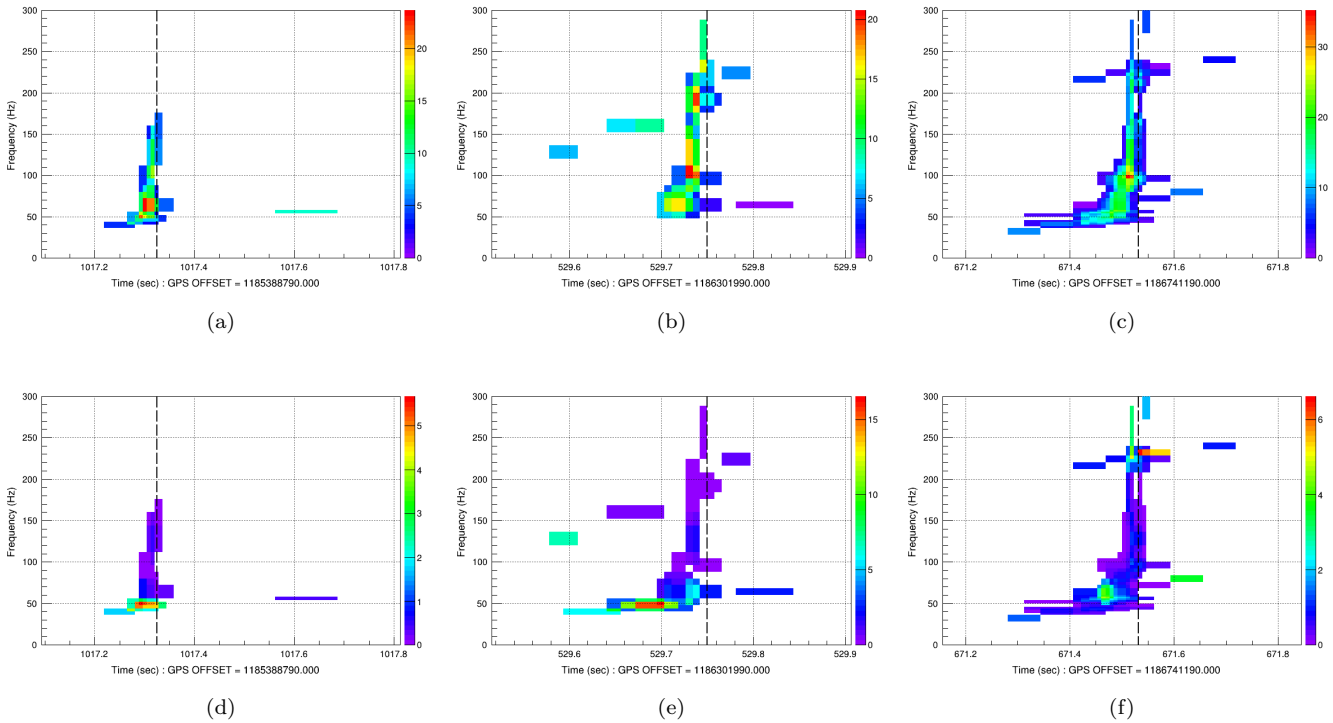

FIG. 1. cWB waveform reconstruction of GW170729, GW170809 and GW170814 in form of time-frequency maps: the coherent network SNR^2 is shown on the first row of plots, while the second is showing the E_N, i.e. the residual noise energy estimated after the reconstructed signal is subtracted from the data; the first column ("a" and "d") refers to GW170729; GW170809 event is shown in the second column ("b" and "e"); finally, the third column reports GW170814 event. The dashed vertical lines show the minR $\mathrm{t}_{\mathrm{L,coa}}$ for these three events (the network reconstruction uses Livingston detector time as a reference).

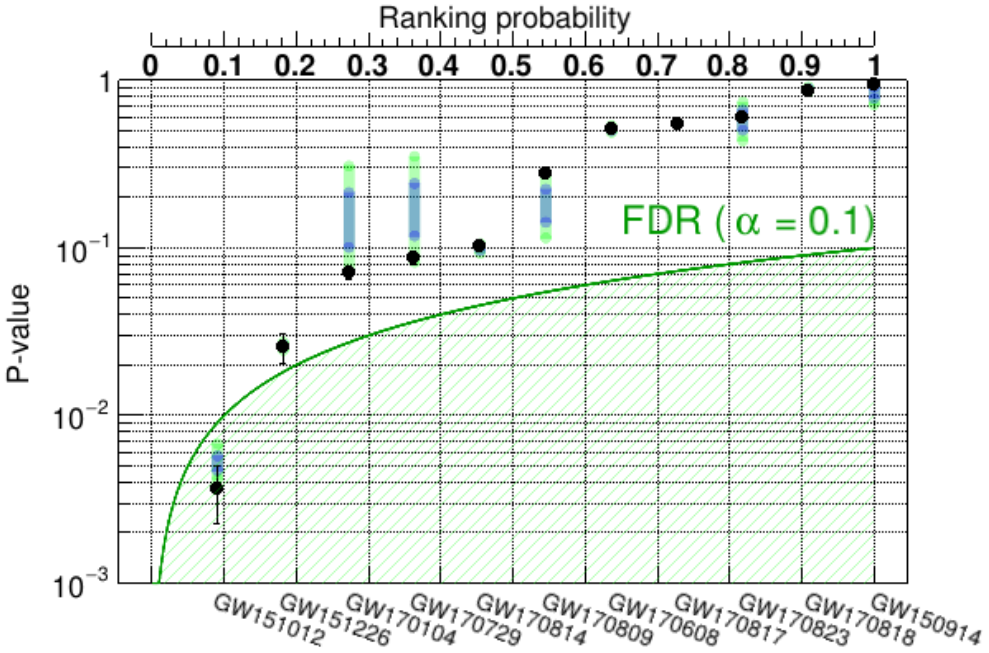

FIG. 2. Sorted p-values of the post-coalescence excesses as a function of the ranking probability (rank/N_{events}), compared with an FDR ($\alpha = 0.1$). Out of the 11 GW events, the post-coalescence $P - value_{pc}$ for GW151012 is an outlier. The second ranked event, GW151226, though mildly significant is consistent with the 11 trials.

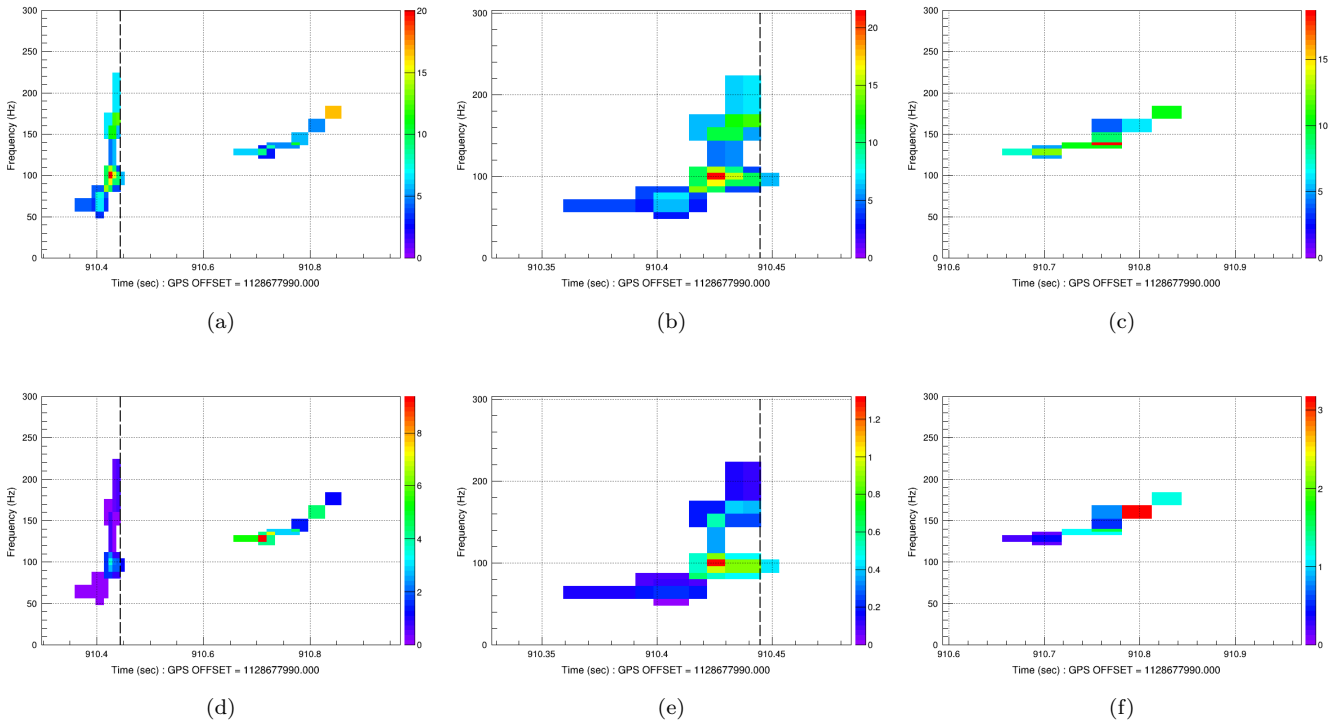

FIG. 3. cWB waveform reconstruction of GW151012, in form of time-frequency maps: the coherent network SNR^2 is shown on the first row of plots, while the second is showing the E_N, i.e. the residual noise energy estimated after the reconstructed signal is subtracted from the data; the first column ("a" and "d") refers to the original reconstruction, with the primary chirp on the left matching the CBC PE reconstruction and a secondary cluster occurring 200 ms after the merger; an ad-hoc time veto covering the secondary cluster was used to produce our best estimate for GW151012 primary event shown in the second column ("b" and "e"); finally, the third column reports the independent reconstruction of the secondary cluster by vetoing the primary event. The dashed vertical lines show the minR $t_{L,coa}$ for GW151012, as the network reconstruction uses Livingston detector time as a reference.

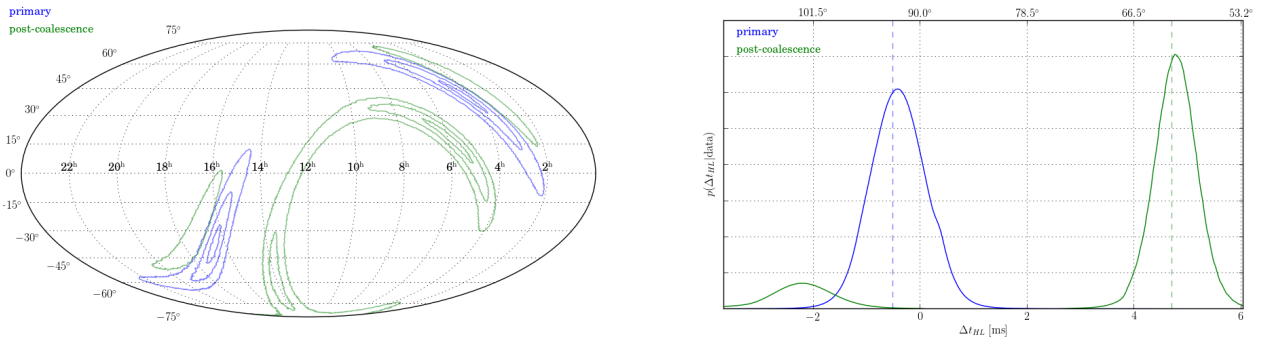

FIG. 4. Mollweide projection of the primary and the secondary events sky reconstructions in equatorial coordinates(a); Time delay MAP marginals between H and L in line-of-sight frame defined by H and L (b). Both figures have been produced using the code in [24].

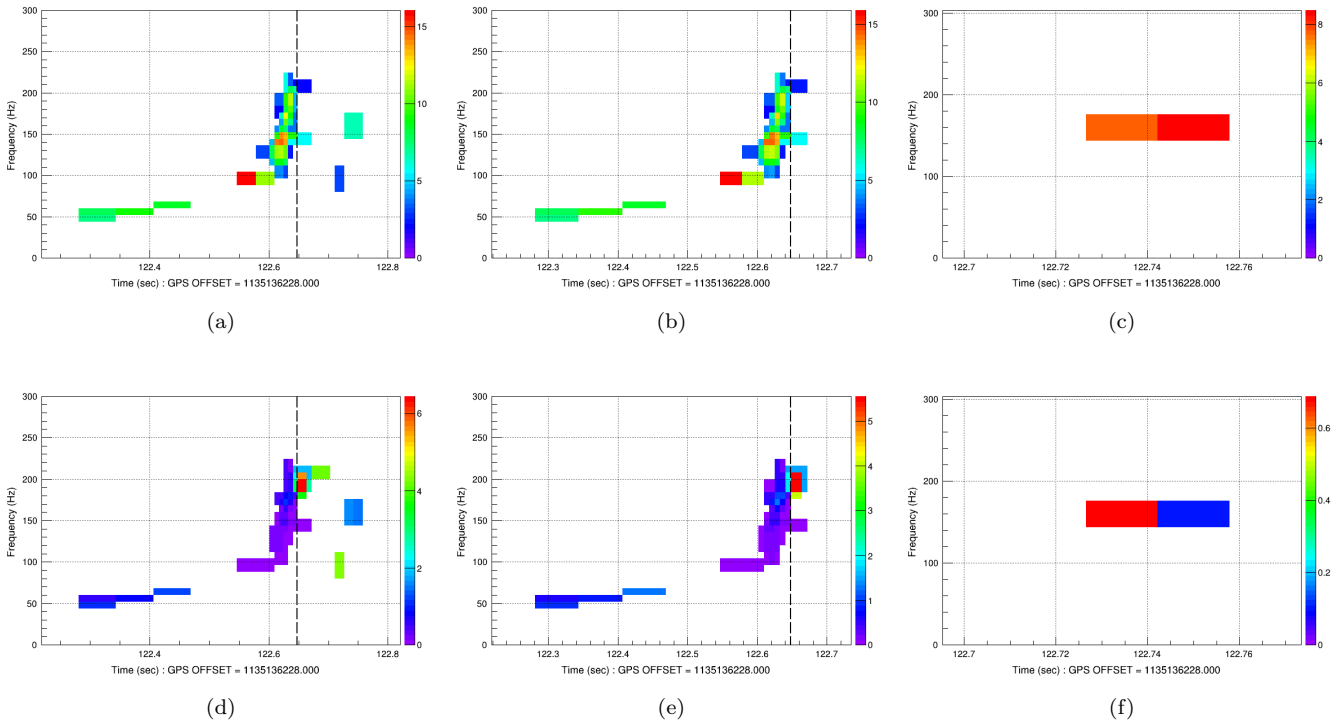

FIG. 5. cWB waveform reconstruction of GW151226, in form of time-frequency maps: the coherent network SNR^2 is shown on the first row of plots, while the second is showing the E_N, i.e. the residual noise energy estimated after the reconstructed signal is subtracted from the data; the first column ("a" and "d") refers to the original reconstruction, with the primary chirp on the left matching the CBC PE reconstruction and a secondary cluster occurring 100 ms after the merger; an ad-hoc time veto covering the secondary cluster was used to produce our best estimate for GW151226 primary event shown in the second column ("b"and "e"); finally, the third column reports the independent reconstruction of the secondary cluster by vetoing the primary event. The dashed vertical lines show the minR $t_{L,coa}$ for GW151012, as the network reconstruction uses Livingston detector time as a reference.

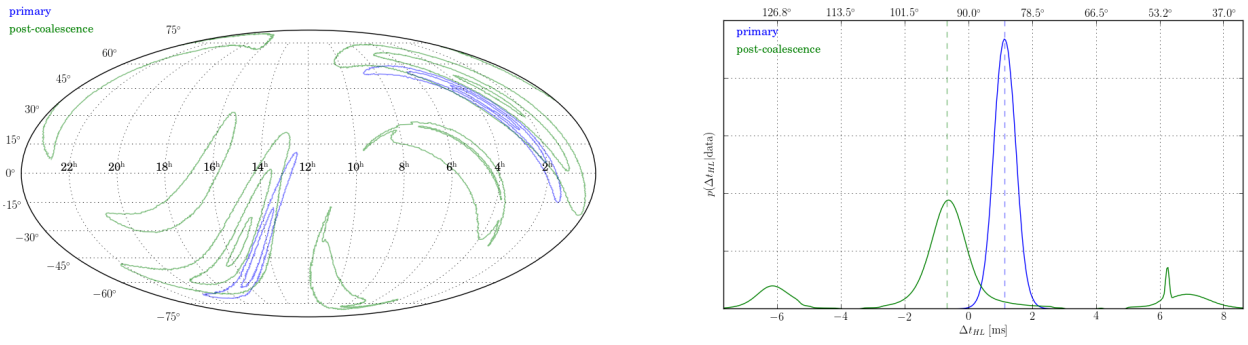

FIG. 6. Mollweide projection of the primary and the secondary events sky reconstructions in equatorial coordinates(a); Time delay MAP marginals between H and L in line-of-sight frame defined by H and L (b). Both figures have been produced using the code in [24].

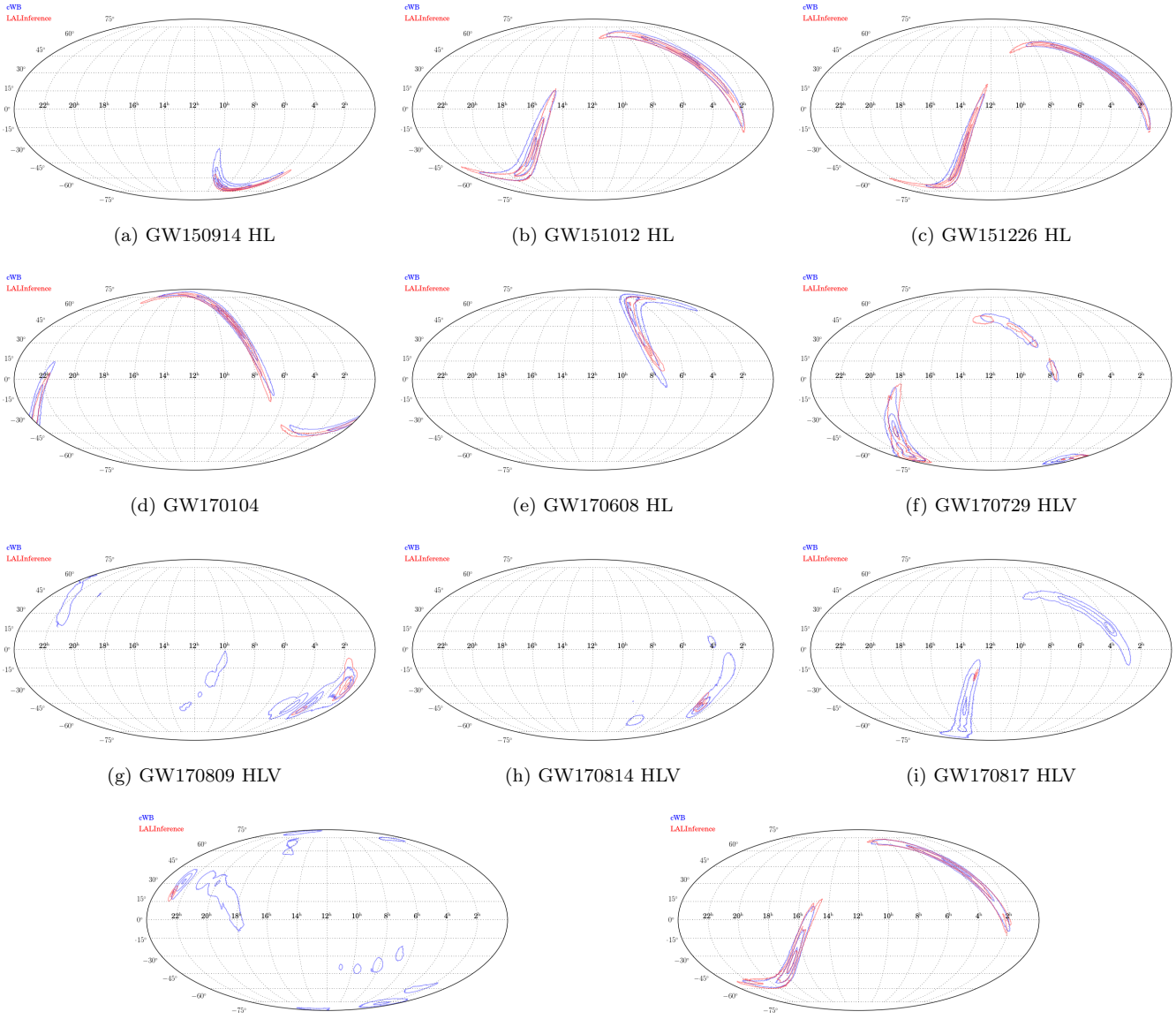

(a) GW150914 HL (b) GW151012 HL (c) GW151226 HL

(d) GW170104 (e) GW170608 HL (f) GW170729 HLV

(g) GW170809 HLV (h) GW170814 HLV (i) GW170817 HLV

(j) GW170818 HLV (k) GW170823 HL

FIG. 7. Mollweide projection of 10%, 50% and 90% credible regions for the sky locations of all GW events as estimated by cWB and LalInference. The probable position of the source is shown in equatorial coordinates. For 5 GW events, i.e. GW170729, GW170809, GW170814, GW170817 and GW170818, the localizations can benefit from the data from a third site, i.e. Virgo. All figures have been produced using the code in [24].